Article

Influence of Axial Linkers on Polymerization in Paddle Wheel Cu(II) Coordination Polymers for the Application of Optoelectronics Devices

Srikanta Jana, Rajkumar Jana, Sayantan Sil, Basudeb Dutta, Hiroki Sato, Partha Pratim Ray, Ayan Datta, Takashiro Akitsu, and Chittaranjan Sinha

Cryst. Growth Des., **Just Accepted Manuscript** • DOI: 10.1021/acs.cgd.9b00764 • Publication Date (Web): 12 Sep 2019

Influence of Axial Linkers on Polymerization in Paddle Wheel Cu(II) Coordination Polymers for the Application of Optoelectronics Devices

Srikanta Jana,[§] Rajkumar Jana,[+] Sayantan Sil,[‡] Basudeb Dutta,[†] Hiroki Sato,[≠] Partha Pratim Ray,*[‡] Ayan Datta,*[+] Takashiro Akitsu,[≠] and Chittaranjan Sinha*[§]

[§]*Department of Chemistry, Jadavpur University, Jadavpur, Kolkata 700 032, India;*

[+]*School of Chemical Sciences, Indian Association for the Cultivation of Science, Jadavpur, Kolkata-32, India;*

[‡]*Department of Physics, Jadavpur University, Jadavpur, Kolkata 700 032, India;*

[†]*Department of Chemistry, Aliah University, New Town, Kolkata 700 156, India;*

[≠]*Department of Chemistry, Faculty of Science, Tokyo University of Science, 1-3 Kagurazaka, Shinjuku-ku, Tokyo 162-8601, Japan.*

ABSTRACT: We have synthesized carboxylato bridged paddle wheel Cu(II) coordination polymers $[Cu_2(DABA)_4(4,4'\text{-BPY})]_n$ (**1**) and $[Cu_4(DABA)_8(PYZ)(H_2O)_2]$ (**2**) by varying axial linkers, 4,4′-Bipyridine (4,4′-BPY) and Pyrazine (PYZ) (HDABA = 4-Diallylamino-benzoic acid). The single crystal X-ray structure of **1** is 1D polymer while **2** is 0D tetranuclear Cu(II) complex. Upon light irradiation the thin film of the compounds increases the electrical conductivity with respect to the dark phase and the conductivity of **1** is ~150 times higher than **2**. Magnetic properties were investigated at an applied field 0.5 T in a temperature range 5–300 K. Compound **1** exhibited ferromagnetic behavior and compound **2** exhibited antiferromagnetic behavior at 300 K and the effective magnetic moment at 300 K, is 1.94 and 0.93 B. M. respectively. The capability to switch photoelectricity and magnetism by changing the crystal structure via axial linker's modification has been rationalized through DFT calculations.

INTRODUCTION

Coordination polymers (CPs)[1-7] have been extensively used in various fields such as in super capacitor,[8] battery,[9] gas storage and separation, sensing[10] and electrocatalysis.[11] But CPs with distinct magnetic and electrical conductivities are of great interest as next-generation functional materials due to their potential applications for electromagnetic interference shielding,[12] biomedicine[13] and microwave absorption.[14] In order to achieve long-range charge transport and strong paramagnetic character, it is crucial for these complexes to have strong intermolecular ordering and strong intramolecular coupling. One of the remarkable features of CP is its ability to adopt different structural architecture under varying conditions. The length of organic spacer and the functional groups of the ligands, the nature of metal ions and the oxidation state along with the reaction condition greatly influence the structure of the CPs. Out of the nine 3d transition metal ions nontoxic Cu(II) (d^9) exhibit a large variation of nuclearity and structures. The magnetic super-exchange interactions between copper centers through the bridging ligands of paddle wheel Cu(II) complexes are well known.[15] But the electrical conductivity and photosensitivity of such type of complexes have not been much investigated. Loh et al.[16] and Zuo et al.[17] reported recently the conductivity and magnetic property of copper based supramolecules.

In this work, we report 1D and 0D paddle wheel Cu(II) complexes, ($[Cu_2(DABA)_4(4,4'\text{-BPY})]_n$ (**1**) and $[Cu_4(DABA)_8(PYZ)(H_2O)_2]$ (**2**)), where DABA acts as carboxylate bridger and BPY, PYZ are N-heterocyclic spacer of similar conjugated π systems with subtle difference in π-acidity and different degrees of σ-donating ability. Selective N-allylation of 4-amino benzoic acid helps to form aliphatic C-H….π interaction which can help single crystal formation. Diallyl group

(have +I effect) of HDABA also increases the electron density on metal centre, which has an effect on conductivity and magnetic properties. These type of CPs are exciting for two main reasons: (i) the paramagnetic Cu(II) (d^9) center and the conducting electrons are linked by a chemical bridge and (ii) the metal is a very good electron transporter between organic linkers.[18] The CPs simultaneously exhibit photosensitive[19] semiconducting nature[20-22] and paramagnetic behavior to make them viable for use in optoelectronic[23], photovoltaic[24] and electromagnetic devices.

RESULTS AND DISCUSSION

Structural analysis of HDABA, $[Cu_2(DABA)_4(4,4'\text{-BPY})]_n$, (1) and $[Cu_4(DABA)_8(PYZ)(H_2O)_2]$, (2)

HDABA crystallizes in the monoclinic C 2/c space group with Z = 8 and exists as a dimer through strong hydrogen bonding with O···H distance 1.80 Å (Fig. 1and Table S1) which has been confirmed by Single-crystal X-ray diffraction experiment.

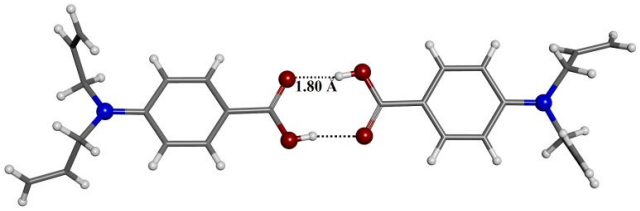

Fig. 1. Dimeric form of 4-Diallylamino benzoic acid.

The structure analyses of **1** and **2** have revealed that the asymmetric unit have identical motif, a discrete carboxylato bridged Cu(II) paddle wheel $[Cu_2(DABA)_4]$ unit which is capped by the N-heterocycles at the axial coordination position. (Fig. 2a and 3a) Both the compounds have distorted square pyramidal geometry around Cu centers with metal…metal interaction, where Cu···Cu distance lies in the range 2.579-2.641 Å. Compound **1** crystallizes in the monoclinic P 21/n space group with Z = 4, where **2** crystallizes in the triclinic P-1 with Z = 1 (Table 1).

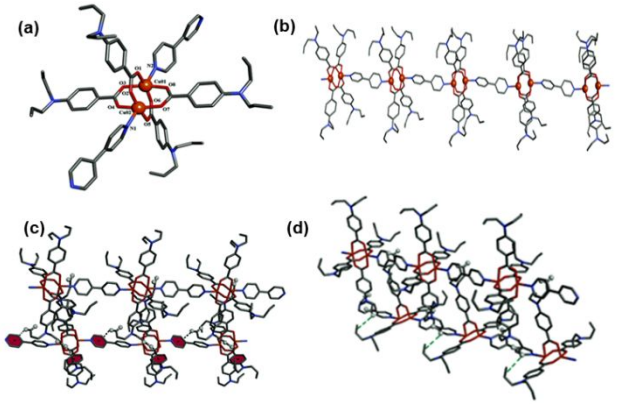

Fig. 2. A portion of the compound 1 displaying the coordination atmospheres of the Cu(II) atoms (a). A schematic diagram displaying the connectivity of the structure (b). A portion of the 2D connectivity displaying C-H…. π interactions (b), (d).

Compound **1** forms 1D polymeric chain by repeating the asymmetric unit and pyridine ring of 4,4'-BPY (Fig. 2b) are twisted along X-axis that may assist efficient charge delocalization through metal orbitals.

Table 1. Crystallographic Data of **1** and **2**.

Compound	Compound-1	Compound-2
CCDC No.	1871434	1871433
Formula	$C_{62}H_{64}Cu_2N_6O_8$	$C_{108}H_{120}Cu_4N_{10}O_{18}$
fw	1148.30	2100.34
crystsyst	monoclinic	triclinic
space group	*P 21/n*	P-1
a (Å)	12.5450(8)	13.1365(11)
b (Å)	34.762(2)	14.0314(12)
c (Å)	13.9615(9)	16.3546(13)
α(deg)	90	66.462(2)
β(deg)	112.248(3)	74.865(2)
γ (deg)	90	87.755(3)
V (Å^3)	5635.2(6)	2660.6(4)
Z	4	1
D_{calcd}(g/cm^3)	1.354	1.311
μ(mm^{-1})	0.816	0.858
λ(Å)	0.71073	0.71073
data[$I > 2\sigma(I)$] /params	9888/703	9295/631
GOF on F^2	1.077	1.122
Final *R* indices[$I > 2\sigma(I)$][a,b]	$R1 = 0.0466$ $wR2 = 0.1180$	$R1 = 0.0479$ $wR2 = 0.1539$

[a] $R1 = \Sigma||F_o| - |F_c||/\Sigma|F_o|$,

[b] $wR2 = [\Sigma w(F_o^2 - F_c^2)^2/\Sigma w(F_o^2)^2]^{1/2}$

The compound **2** forms tetranuclear Cu(II) complex and water molecules act as capping ligands. These coordinating water molecules enables strong hydrogen bonding with bridging carboxylate groups with O···O distances in the range ~2.8 Å leading to the formation of the 1D polymeric network (Fig. 3b). These complexes are capable of forming higher dimensional structures through H-bonding and Supramoleculer[25] (aliphatic, aromatic C-H….π) interactions (3.066–3.454 Å, (Fig. 2c-d, 3c- d and Fig. S1).

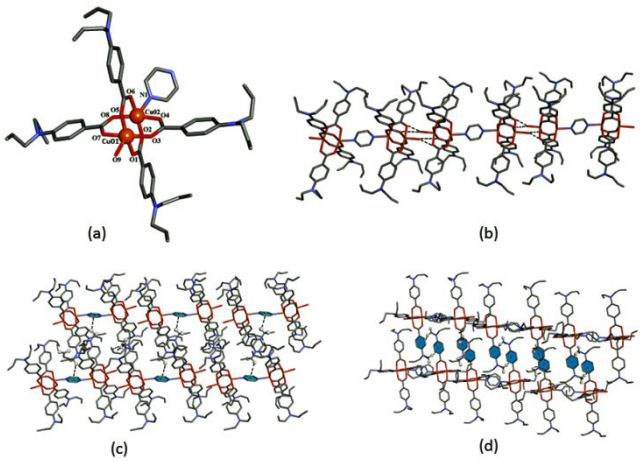

Fig. 3. A portion of the compound 2 displaying the coordination atmospheres of the Cu(II) atoms (a). A portion of the 2D connectivity displaying hydrogen bonding interactions (b).). A portion of the 2D connectivity displaying C-H…. π interactions (c), (d).

The intramolecular N-N distance in the heterocyclic bridger (in 4,4′-BPY of **1** it is 7.08 Å much longer than 2.75 Å in PYZ of **2**) may be the major driving force for the formation of 1D superstructure for **1** and 0D for **2**. Smaller size of PYZ allows large steric hindrance and may not permit the formation of 1D polymeric chain in **2**.

Single-crystal X-ray diffraction data is well supported by density functional theory (DFT) study, performed using plane –wave technique as implemented in Vienna Ab Initio Simulation Package (VASP) (details are given in supporting information).

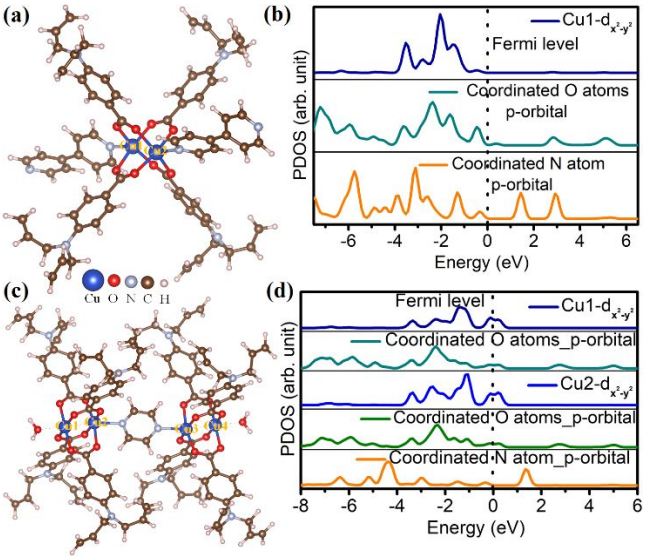

Fig. 4. Optimized structures of compound **1** (a) and **2** (c), PDOS plots for Cu-$d_{x^2-y^2}$ and p-orbitals of Cu coordinated oxygen and nitrogen atoms in compound **1** (b) and **2** (d).

Cu···Cu distances (in the range 2.579-2.641 Å) determined from the SC-XRD experiment is also well matched with DFT optimized structures which show Cu···Cu distances are 2.70 and 2.56 Å respectively for compound 1 and 2 (Fig. 4a and c). In accordance with SC-XRD, DFT optimized structures reveals Cu1 center in compound **1** is coordinated with four oxygen atoms of the carboxylato groups (Cu-O bond length ~2.0 Å) and one nitrogen atom from N-heterocycle (Cu-N bond length ~2.28 Å) whereas in compound **2** Cu1 center is covalently linked with four oxygen atom of the carboxylato groups (Cu-O ~ 2.05Å) and one oxygen atom from water through hydrogen bonding interaction (Cu···O ~ 2.33Å). On the other hand Cu2 center in compound **2** shows bonding interaction with four oxygen atoms of the carboxylate groups (Cu-O ~ 2.03Å) and one nitrogen atom from N- heterocycle (Cu-N ~ 2.23 Å). Projected density of states (PDOS) analysis clearly reveals that the bonding interaction between Cu and coordinated atoms originates from Cu-$d_{x^2-y^2}$ orbitals and p-orbitals of nitrogen and oxygen atoms both in compound **1** and **2** (Fig. 4 b-d).

TGA and PXRD analysis

Thermogravimetric analysis (TGA) of bulk of the compounds has suggested that compound **2** is thermally less stable (decomposition starts at 200 °C) comparing with **1** (decomposition starts at 250 °C) (Fig. S2). Lowering of thermal stability of **2** may be due to inferior dimensionality (0D) compared to **1** (1D) and the presence of coordinated water molecule in the structure. All of the major peaks of PXRD patterns of bulk matched quite better with those simulated from single crystal data which also establish the phase pureness of the bulk (Fig. S3 and S4).

MAGNETIC PROPERTIES

Paddle-wheel copper(II) carboxylato CPs [Cu(II), d^9] are well-known to possess magnetic super exchange interactions[26] between the two copper(II) centers through the bridging ligands. The extent of the exchange interaction is known to be controlled by several factors, including the geometry of the Cu(II) ions, the bond angles and the bond lengths of the bridging atoms, the bridging mode of the ligand and also the type of bridging linkers[27,28] (Table S2 and S3). The spin super-exchange interaction of the binuclear copper(II) complexes can be understood in terms of the natural (non-orthogonalized) magnetic orbitals.[29-31] At 300 K, the effective magnetic moment for **1**, and **2** are 1.94, and 0.93 B.M., respectively, which correspond to spin only values of S=1/2 for Cu(II) (1.73 B. M.). It is noted that the effective magnetic moment of compound **1** is greater than that of single uncoupled Cu(II) ion and compound **2** shows much less value than that of one-electron spin uncoupled Cu(II) ion. The compound **1** exhibits $\chi_A T$ value 0.0223 emu K/(Oe . mol) at 5 K and is increased linearly upto 20 K followed by sigmoidal change in the

$\chi_A T$ value to 0.472 emu K/(Oe . mol) at 300 K (Fig. 5). For compound **2** $\chi_A T$ becomes 0.0098 emu K/(Oe . mol) at 5 K and follows paramagnetic change ($\chi_A T$ vs T is linear) upto 100 K.

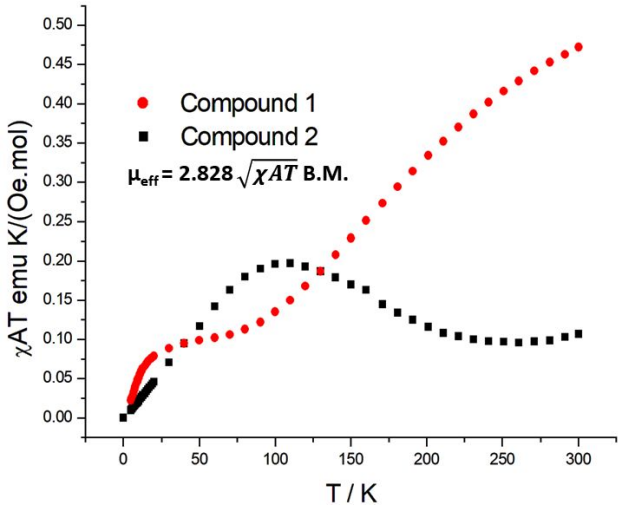

Fig. 5. Variation of $\chi_A T$ value with temperature for compounds **1** and **2** (where χ_A refers to diamagnetic correction of χ_M).

Then it is gradually decreased until around 250 K and the $\chi_A T$ value is reached to 0.107 emu K/(Oe . mol) at 300 K (Fig. 5). Therefore, compound **1** becomes ferromagnetic at room temperature while the compound **2** is antiferromagnetic at 300 K. To further rationalize the strong antiferromagnetic coupling interactions between the Cu^{2+} ions as well as among the covalently linked atoms with Cu^{2+} ions (coordinated N and O atoms) at low temperature, we have performed DFT and calculated magnetic moment values at low temperature (~0 K) for both the compounds **1** and **2**.

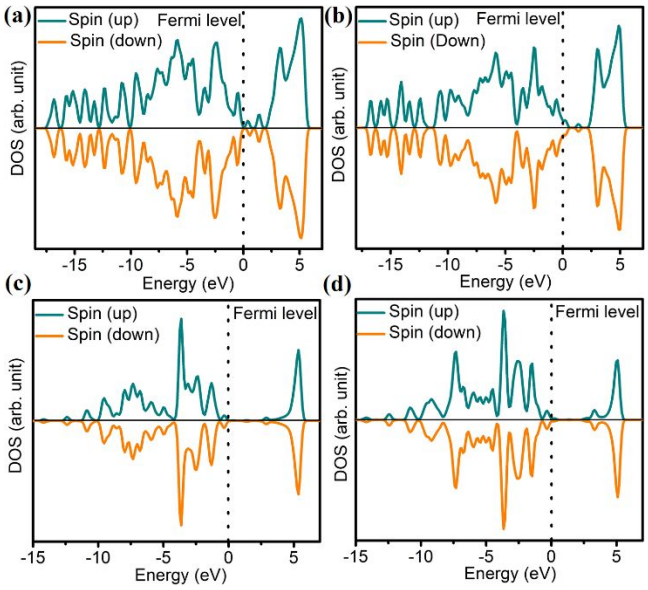

Fig. 6. DOS plots for (a) compound 1 (b) compound 2, LDOS plots for Cu^{2+} ions in compound 1 (c) and 2 (d).

Charge transfer from Cu^{2+} ions to the ligand orbitals results ferromagnetic coupling in the ambient temperature. DFT calculations on both compounds **1** and **2**, reveal that strong charge transfer from coordinated atoms to Cu^{2+} centers (~0.9 e on average for both compounds) results in strong anti-ferromagnetic coupling with the more localization of electrons on Cu^{2+} centers (magnetic moment = 0.000 μB) at low temperature (~0K) (Table S4). The anti-ferromagnetic coupling phenomenon is well understood from total as well as localized density of states (TDOS, LDOS) analysis (Fig. 6). The perfectly symmetric nature of electron density of spin up and down clearly indicates that there are strong antiferromagnetic coupling interactions among the Cu^{2+} ions as well as between Cu^{2+} and coordinated ligands (Fig. 6a-b) for compounds **1** and **2**. The LDOS of Cu^{2+} ions and coordinated nitrogen and oxygen atoms of compounds **1** and **2** clearly demonstrates that the spin on the atoms are all antiferromagnetically coupled (Fig. 6c-d and Fig. S5a-c).

Apart from this, d^9 configuration of Cu(II) being more than half-filled has significant orbital contribution and also the presence of hydrogen bonding and other supramolecular interactions can also influence the magnetic properties.[32]

ELECTRICAL CHARACTERIZATION

Impedance Spectroscopy study and current-voltage (I-V) measurement

Impedance Spectroscopy (IS) study is performed in frequency range 40 Hz-10 MHz at room temperature. Fig. 7a shows the Nyquist plot for two compounds in the dark condition. The higher frequency semicircular arc depicts the bulk contribution and intermediate or low frequency semicircular arc represents the grain-boundary or electrode-specimen effect.[33] The intercept of the semicircular arc on real axis Z' depicts the bulk resistance R_b (dc resistance) of the sample. From Fig. 7a and inset of Fig. 7a, it is clearly seen that compound **1** has lower resistance than compound **2**.

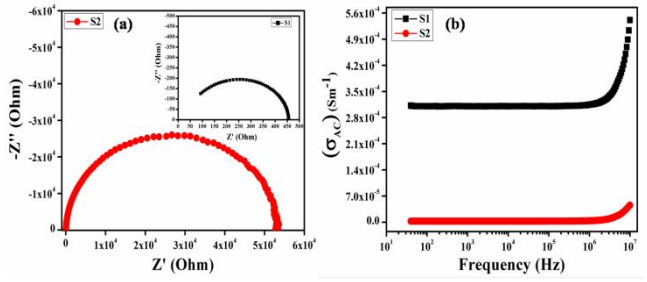

Fig. 7. (a) Nyquist plot and (b) frequency dependent ac conductivity plot for compounds **1** and **2**.

The lower resistance signifies the better possibility of charge transfer. Fig. 7b represents ac conductivity vs. frequency (log scale) plot for compound **1** and **2**. At lower frequency region, the extrapolation of Y-axis gives the value of dc conductivity (σ_{DC}), which is attributed to the long range translational motion of the charge carriers. In high frequency region the term $A\omega^n$ is responsible for the frequency dependent behaviour and the dispersion nature.[34] The frequency dependence of ac conductivity (σ_{AC}) may be because of free and bound carriers.[35] The frequency dependent conductivity can be expressed by the following power law equation .[36, 37]

$$\boldsymbol{\sigma(\omega) = \sigma_{dc} + \sigma_{ac}} \qquad (1)$$

Where, $\sigma(\omega)$ is the total conductivity, σ_{DC} is the dc conductivity and σ_{AC} is the ac conductivity. At high frequency region, the increase of conductivity described through Jonscher's power law [1] and it is defined as:

$$\boldsymbol{\sigma_{ac} = \sigma_{dc}[1 + (\frac{\omega}{\omega_H})^n]} \qquad (2)$$

Where, n is the dimensionless frequency component, ω ($\omega=2\pi f$) is the angular frequency and ω_H is the hopping frequency of the charge carrier. At room temperature, the dc conductivity (σ_{DC}) of the compound **1** and **2** are calculated as 3.12×10^{-4} Sm^{-1} and 2.65×10^{-6} Sm^{-1} respectively which was also verified by computationally and the corresponding theoretical band gap are 1.36 eV and 1.75 eV respectively (Fig. S7). The DFT calculated DC electrical current conductivity ($\sigma_{dc,\ DFT}$) of the compound **1** is 1.1×10^{-4} whereas that of compound **2** is 8.5×10^{-7} Sm^{-1} that agrees with the experimentally determined electrical conductivity value. Both the experimental and DFT study shows that compound **1** is more conducting (in order of magnitude) compared to compound **2**. Motivated from these results, the current-voltage (I-V) characteristics of Al/Compound/ITO sandwich structure have been performed within the voltage range ±1V.

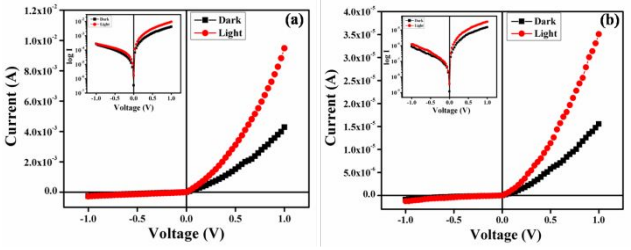

Fig. 8. Current-Voltage (I-V) characteristic curves for (a) compound 1 and (b) compound 2 under dark and light condition.

Fig. 8a-b shows the current-voltage characteristic curves of devices (compound **1** and **2**) in the dark/under irradiation with white light (irradiance ~ 1000 Wm^{-2}). Fig. 8 shows that the fabricated devices based on the samples exhibit non-linear rectifying behavior, similar to the Schottky diode behavior. The rectification ratio (i.e., On/Off ratio) of the devices in the dark/under illumination condition are found to be 16.00, 17.39 and 34.64, 28.25 for the compound **1-2** respectively. Logarithmic presentation of I as a function of V is shown in inset of Fig. 8.

We have analyzed the I-V characteristic curves by introducing standard thermionic emission (TE) theory[38] for exploring the charge transport phenomena by considering the following standard equations. [39]

$$\boldsymbol{I = I_0 exp\left(\frac{qV}{\eta KT}\right)\left[1 - exp\left(\frac{-qV}{\eta KT}\right)\right]} \qquad (3)$$

Where, I_0 is the saturation current derived from the straight line intercept of ln (I) at V= 0 and is given by

$$\boldsymbol{I_0 = AA^* T^2 exp\left(\frac{-q\emptyset_B}{KT}\right)} \qquad (4)$$

Where, q stands for the electronic charge, k is the Boltzmann constant, T is the temperature in Kelvin, V is the forward bias voltage, A is the effective diode area, η is the ideality factor and A* is the effective Richardson constant respectively. The effective diode area is estimated as 7.065×10^{-6} m^2 and the effective Richardson constant is considered as 1.20×10^6 $AK^{-2}m^{-2}$ for all the devices. At low bias, linearity in current is observed which is consistent with Eq. (3), while the deviation from linearity at higher bias voltages occurred due to the change in diode series resistance. From Cheung, the forward bias I-V characteristics in term of series resistance can be expressed as,[40]

$$\boldsymbol{I = I_0 exp\left[\frac{q(V - IR_S)}{\eta kT}\right]} \qquad (5)$$

Where, the IR_S term is the voltage drop across series resistance of device.

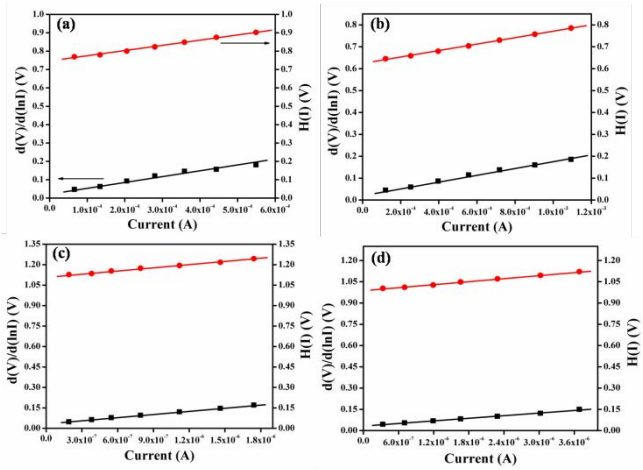

Fig. 9. dV/d(lnI) vs. I and H(I) vs. I curve for compound 1 and 2 based Schottky barrier diode under dark (a), (c) and photo (b), (d) condition.

In this circumstance, the values of the series resistance can be determined from following functions using equation (5) [41]

$$\boldsymbol{\frac{dV}{dln(I)} = \left(\frac{\eta KT}{q}\right) + R_S I} \qquad (6)$$

$$\boldsymbol{H(I) = R_S I + \eta\emptyset_B} \qquad (7)$$

and H(I) can be represented as:

$$\mathbf{H(I) = V - \left(\frac{\eta KT}{q}\right)ln\left(\frac{I}{AA^{*}T^{2}}\right)} \qquad (8)$$

The plot of dV/dln(I) vs. I gives the value of series resistance (R_S) as the slope and the ideality factor (η) as the y-axis intercept. The dV/dln(I) vs. I graph for all devices in the dark/under light condition have been portrayed in Fig. 9. The potential barrier height for all devices are evaluated from the y-axis intercept of H(I) vs I curve (Fig. 9). The slope of this plot also furnishes a second determination of the series resistance. The obtained values of ideality factor, barrier height and series resistance are listed in Table-S5. The values of ideality factor (η) in the dark condition deviated from ideal behavior and this difference is due to the presence of inhomogenities of Schottky barrier height, high probability of electron and hole recombination in the depletion region, existence of interface states and series resistance.[42,43] But, under the illumination of light the value of ideality factor approaches unity. Series resistance (R_S) of all the compounds in both cases decrease after soaking light, these results indicate a certain reduction in carrier density in the depletion region of the rectifier through the introduction of traps and recombination centres associated with illumination effect, which signifies its applicability in the field of optoelectronics devices.

For a better insight into the charge transport phenomena through the metal-semiconductor (MS) junction, we investigate the forward I-V curves in details by employing the space charge limited current (SCLC) theory.

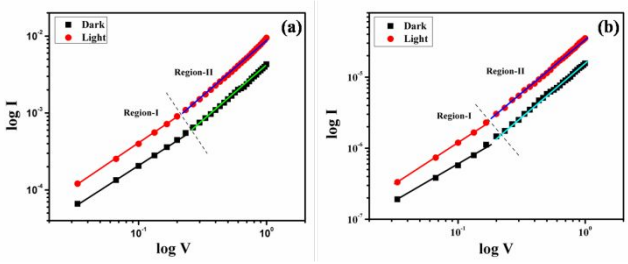

Fig. 10. log I versus log V plot for (a) compound 1 and (b) compound 2 under dark and light condition.

The characteristic I-V curves in the dark/under light conditions in the logarithmic scale portrayed in Fig. 10. Fig. 10 clearly demonstrates two regions with different slopes, indicating different conduction mechanisms. The current conduction mechanism is governed by the power law ($I \propto V^m$), [44] where m is the slope of the I vs. V curve. At low bias voltage (region-I), the sample exhibits an ohmic behavior, i.e., the current is directly proportional to the applied bias voltage ($I \propto V$). The I-V characteristics in this region can be attributed due to the thermionic emission and the current is dominated by bulk generated electrons of the film, rather than the injected free carriers.[45] The region II corresponds to the higher ordered magnitude of slope, exhibits variation of current with square of forward bias voltage ($I \propto V^2$). In this region the current is governed by space charge, designated as space charge limited current (SCLC).[46] The trap distribution is the key factor in this type of charge transport mechanism.

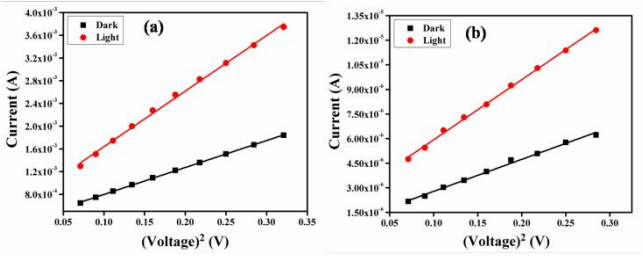

Fig. 11. I vs V^2 plot of SCLC region under dark and photo condition for (a) compound 1 and (b) compound 2.

As the traps are exponentially distributed in this region, current increases rapidly. Moreover, to check the performance of the devices effective carrier mobility are evaluated from I vs V^2 plot (Fig. 11) from the SCLC region, by evaluating the slope with the help of Mott-Gurney space-charge-limited-current (SCLC) equation.[47, 48]

$$\mathbf{I = \frac{9\mu_{eff}\varepsilon_0\varepsilon_r A}{8}\left(\frac{V^2}{d^3}\right)} \qquad (9)$$

Where, I is the current, ε_0 is the permittivity of free space and ε_r the dielectric constant.

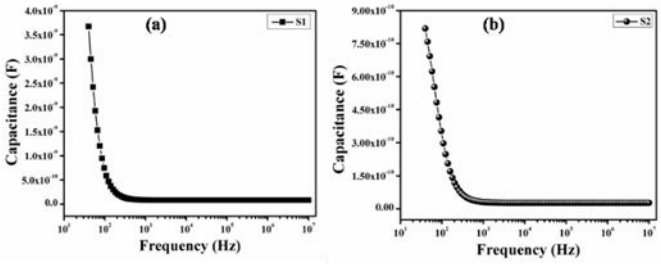

Fig. 12. Capacitance versus frequency plot for (a) compound 1 and (b) compound 2.

The value of dielectric constant of the material is measured from capacitance versus frequency plot (C-f) (Fig. 12) with the help of following equation:[49]

$$\varepsilon_r = \frac{Cd}{\varepsilon_0 A} \qquad (10)$$

Where, C is the capacitance (at saturation), d is the thickness and rest are same as defined previously. We have also theoretically determined dielectric constant of the compound **1** and **2**. Compound **1** has dielectric constant of 1.36 while for the compound **2** it is 1.25 which agrees well with the experimentally determined dielectric constants. The frequency dependent dielectric constant plot has been given in the supporting information (Fig. S6). Mobility and transit time are the prime factor to determine the device performance. Transit time (τ) is defined as the time required by a

carrier to travel from anode to cathode. It can be expressed as the summation of average total time spent by each electron as a free carrier plus total time spent in the tarp.[50] The transit time (τ) of the charge carrier is deduced by using the equation: [51]

$$\tau = \frac{9\varepsilon_0\varepsilon_r A}{8d}\left(\frac{V}{I}\right) \qquad (11)$$

The effective mobility of the carriers under dark condition is evaluated as 5.21×10^{-5} $m^2V^{-1}s^{-1}$ and 6.48×10^{-7} $m^2V^{-1}s^{-1}$ for compound **1** and **2**. After irradiation of light the values of effective carrier mobility (μ_{eff}) improved to 1.07×10^{-4} $m^2V^{-1}s^{-1}$ and 1.21×10^{-6} $m^2V^{-1}s^{-1}$ for those compounds respectively. Longer transit time in dark condition leads to higher trapping probabilities[52] but after illumination of light the situation is reverse due to the higher carrier mobility. The values of effective carrier mobility and transit time of compound **1** and **2** based devices are tabulated in Table-S6. Hence, compound **1** is better candidate than compound **2** for the application in photovoltaic devices.

EXPERIMENTAL SECTION

Materials and general method

Sigma Aldrich helped us by providing all the required chemicals. Micro–analytical data (C, H, N) were collected on Perkin- Elmer 2400 CHNS/O elemental analyzer. Thermogravimetric analysis was recorded on a Perkin–Elmer Pyris Diamond TG/DTA in the temperature range between 30 °C and 600 °C under a nitrogen atmosphere at a heating rate of 12 °C min^{-1}. Single crystal of the compound 1 and 2 was used for data collection using a Bruker SMART APEX II diffractometer equipped with graphite-monochromated MoKα radiation (λ = 0.71073 Å). The crystal structure was solved using the SHELX-97 package. The PXRD data was collected on a Bruker D8 Advance X-ray diffractometer using Cu Kα radiation (λ = 1.548 Å) generated at 40 kV and 40 mA. The PXRD spectrum was recorded in a 2θ range of 5–50. Magnetic properties were investigated using a Quantum Design MPMS-XL superconducting quantum interference device magnetometer (SQUID) at an applied field 0.5 T in a temperature range 5–300 K. The diamagnetic correction was carried out by using Pascal constants. The di-electrical study was carried out by evaluating capacitance (C), impedance (Z),and phase angle (θ) of the sample as a function of frequency (40 Hz–10 MHz) using a computer-controlled Agilent make precision 4294A LCR meter. The Current-Voltage (I-V) characteristics of two devices are recorded under dark and light (AM 1.5 radiation) condition with the help of Keithley 2635B source meter interfaced with PC by applying bias voltage in the range of -1 V to +1 V. All the measurements are performed at room temperature.

Synthesis of 4-Diallylamino-benzoic acid allyl ester

Allylations of 4-amino benzoic acid were carried out by using the literature procedure.[53] The obtained white solid (2.347 g, 97%) was recrystallized from methanol and tri allylation was characterised by ^{1}H NMR spectrum. ^{1}H NMR (300 MHz, CDCl3): d 3.94 (d, 4H), d 4.75 (d, 2H), d 5.20 (m, 4H), d 5.33 (m, 2H), d 5.81 (m, 2H), d 6.01 (m, 1H), d 6.60 (m, 2H), d 7.90 (d, 2H):(Fig. S9)

Synthesis of 4-Diallylamino-benzoic acid

We have synthesized these reported compound[54] with modified procedure. Selective deallylation of 4-Diallylamino-benzoic acid allyl ester was carried out using the following procedure. To a 250 mL round bottom flask the 4-Diallylamino-benzoic acid allyl ester (2.347 g 9.72 mmol) was dissolved in a solution of NaOH (3.11 g, 8 equiv) in 50 mL MeOH and 50 mL H_2O and stirred at room temperature for 12 h. The reaction mixture was then acidified with 6N HCl, white precepited comes out, filtered and residue was recrystallized from methanol, gives pure **4-**Diallylamino-benzoic acid (2.015, g 95%). ^{1}H NMR (300 MHz, CDCl3): d 3.99 (d, 2H), d 5.20 (m, 4H), d 5.83 (m, 2H), d 6.64 (d, 2H), d 7.92 (d, 2H,): (Fig. S10).

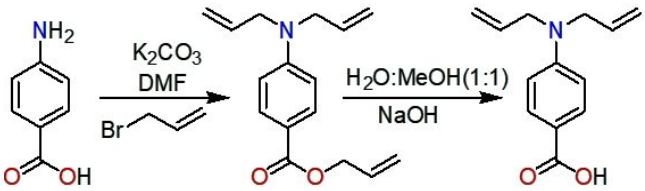

Fig. 13. Schematic representation of the preparation of 4-Diallylamino-benzoic acid.

Synthesis of compound 1 and 2

A methanolic solution of (1 ml) of 4,4-BPY (15.619 mg, 0.1 mmol) was carefully layered by the help of water-metahnol mixed solvent over the aqueous solution of (1 ml) of $Cu(NO3)_2,3H_2O$, (24.16 mg, 0.1 mmol). HDABA (21.726 mg, 0.1 mmol) in ethanol (1 ml) was neutralized with Et_3N (10.119 mg, 0.1 mmol) and was layered cautiously over the 4,4-BPY followed by water-metahnol mixed solvent to make an undisturbed layer. It was then allowed to diffuse for a week. The blue coloured needle-shaped crystals were deposited on the glass wall. The crystals were separated mechanically under a microscope and washed with methanol and water (1:1) mixture, and dried. The yield of $[Cu_2(DABA)_4(4,4'\text{-BPY})]_n$, **1** was 75 % (45.934 mg). Elemental analysis calculated for (**1**); C, 58.23; H, 9.46; N, 7.75%.

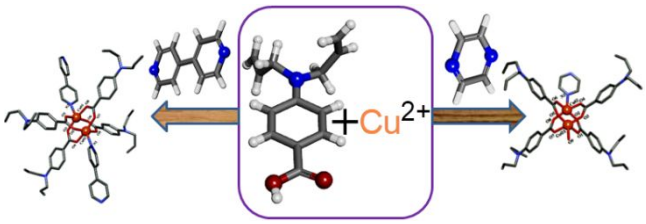

Fig. 14. Schematic representation of the preparation of the compound **1** and **2**.

The same synthetic procedure has been applied for compound **2** as adopted for **1**, except PYZ (8.009 mg, 0.1 mmol). The blue coloured block-shaped crystals were deposited on the glass wall. The yield of $[Cu_4(DABA)_8(PYZ)(H_2O)_2]$**, 2** was 80 % (43.158 mg). Elemental analysis calculated for (**2**); C, 59.23; H, 9.74; N, 6.42 %.

CONCLUSIONS

We have successfully synthesized two structurally distinct Cu based coordination polymers having 1D and 0D structures respectively with fascinating electrical and magnetic properties. These properties can be further tailored by modifying the axial linkers. Tuning of axial linkers leads to the formation of charge transfer complexes which significantly enhances its magnetic moment and improves its electrical properties.

ASSOCIATED CONTENT

Supporting Information (SI)

Supplementary structures of the compounds **1** and **2**, Fabrication of Schottky diodes, PXRD, TGA, detail DFT computation, NMR, (Fig. S1-S10); detail of X-ray crystallographic measurements, detail bond parameters, Schottky Diode Parameters, Charge Transport Parameters, (Table S1-S7), CCDC No. 1871615; 1871434; 1871433. This material is available free of charge via the Internet at http://pubs.acs.org.

AUTHOR INFORMATION

Corresponding Authors

*E-mail: partha@phys.jdvu.ac.in

*E-mail: crsjuchem@gmail.com

*E-mail: spad@iacs.res.in

ORCID

Chittaranjan Sinha: 0000-0002-4537-0609

Partha Pratim Ray: 0000-0003-4616-2577

Ayan Datta: 0000-0001-6723-087X

ACKNOWLEDGMENTS

Financial support from the Council of Scientific and Industrial Research (CSIR, Sanction no. 01(2894)/17/EMR-II), New Delhi, India is gratefully acknowledged. S. J thanks the CSIR, New Delhi for fellowship.

REFERENCES

(1) Batten, S. R.; Neville, S. M.; Turner, D. R. Coordination Polymers. Design, Analysis and Application, *Royal Society of Chemistry*, London, **2009**.

(2) Desiraju, G. R.; Vittal, J. J.; Ramanan, A. *Crystal Engineering*. A Textbook, World Scientific, Singapore, **2011**.

(3) Zhou, H.-C.; Long, J. R.; Yaghi, O. M. Introduction to Metal−Organic Frameworks. *Chem. Rev*. **2012**, *112*, 673–674.

(4) Moulton, B.; Zaworotko, M. J. From Molecules to Crystal Engineering: Supramolecular Isomerism and Polymorphism in Network Solids. *Chem. Rev*. **2001**, *101*, 1629–1658.

(5) Natarajan, S.; Mahata, P.; Sarma, D. J. The relevance of metal organic frameworks (MOFs) in inorganic materials chemistry. *Chem. Sci*. **2012**, *124*, 339–353.

(6) Biradha, K.; Su C.-Y.; Vittal, J. J. Recent Developments in Crystal Engineering. *Cryst. Growth. Des*. **2011**, *11* , 875–886.

(7) Kitagawa, S.; Kitaura, R.; Noro, S.-I. Functional Porous Coordination Polymers. *Angew. Chem*. Int. Ed. **2004**, *43*, 2334–2375.

(8) Choi, K. M.; Jeong, H. M.; Park, J. H.; Zhang, Y.; Kang, J. K.; Yaghi, O. M. Supercapacitors of nanocrystalline metal-organic frameworks. *ACS Nano*. **2014**, *8*, 7451-7457.

(9) Férey, G.; Millange, F.; Morcrette, M.; Serre, C.; Doublet, M.; Grenèche, J.; Tarascon, J. Mixed-Valence Li/Fe-Based Metal–Organic Frameworks with Both Reversible Redox and Sorption Properties. *Angew. Chem. Int. Ed.* **2007***, 46,* 3259-3263.

(10) Campbell, M. G.; Sheberla, D.; Liu, S.; Swager, T. M.; Dincă, M. Cu_3(hexaiminotriphenylene)$_2$: an electrically conductive 2D metal-organic framework for chemiresistive sensing. *Angew. Chem. Int. Ed*. **2015**, *54*, 4349-4352.

(11) Nohra, B.; Moll, H. E.; Albelo, M. R.; Mialane, P.; Marrot, J.; Mellot-Draznieks, C.; O'Keeffe, M.; Biboum, R. N.; Lemaire, J.; Keita, B.; Nadjo, L.; Dolbecq, A. Polyoxometalate-Based Metal Organic Frameworks (POMOFs): Structural Trends, Energetics, and High Electrocatalytic Efficiency for Hydrogen Evolution Reaction. *J. Am. Chem. Soc*. **2011**, *133*, 13363-13374.

(12) Bayat, M.; Yang, H.; Ko, F. K.; Michelson, D.; Mei, A. Electromagnetic interference shielding effectiveness of hybrid multifunctional Fe3O4/carbon nanofiber composite. *Polymer*. **2014**, *55*, 936-943.

(13) Wuang, S. C.; Neoh, K. G.; Kang, E.-T.; Pack, D. W.; Leckband, D. E. Synthesis and functionalization of polypyrrole-Fe3O4 nanoparticles for applications in biomedicine. *J. Mater. Chem*. **2007**, *17*, 3354-3362.

(14) Zhang, D. Q.; Cheng, J. Y.; Yang, X. Y.; Zhao, B.; Cao, M. S. Electromagnetic and microwave absorbing properties of magnetite nanoparticles decorated carbon nanotubes/polyaniline multiphase hetero structures. *J. Mater. Sci*. **2014**, *49*, 7221-7230.

(15) Mohideen, M. I. H.; Lei, C.; Tuc˘ek , J.; Malina, O.; Brivio, F.; Kasneryk,V.; Huang, Z.; Mazur, M.; Zou , X.; Nachtigall, P.; C˘ejkaa, J.; Morris, R. E. Magneto-structural correlations of novel kagome´-type metal organic frameworks. *J. Mater. Chem. C*. **2019**, *7*, 6692-6697.

(16) Sengupta, A.; Datta, S.; Su, C.; Herng, T. S.; Ding, J.; Vittal, J. J.; Loh, K. P. Tunable Electrical Conductivity and Magnetic Property of the Two Dimensional Metal Organic Framework [Cu(TPyP)Cu2(O2CCH3)4]. *ACS Appl. Mater. Interfaces.* **2016**, *8*, 16154−16159.

(17) Yu, F.; Kurmoo, M.; Zhuang, G.-L.; Zuo, J.-L. Hierarchical tandem assembly of planar [3×3] building units into {3×[3×3]} oligomers: mixed-valency, electrical conductivity and magnetism. *Chem. Sci*. **2018**, *9*, 7498.

(18) Benbellat, N.; Gavrilenko, K.. S.; Gal, Y. L.; Cador, O.; Golhen, S.; Gouasmia, A.; Fabre, J.-M.; Ouahab, L. Co(II)−Co(II) Paddlewheel Complex with a Redox-Active Ligand Derived from TTF. *Inorg. Chem*. **2006**, *45*, 10440-10442.

(19) Dutta, B.; Das, D.; Datta , J.; Chandra, A.; Jana, S.; Sinha, C.; Ray , P. P.; Mir, M. H. Synthesis of a Zn(II)-based 1D zigzag coordination polymer for the fabrication of optoelectronic devices with remarkably high photosensitivity. *Inorg. Chem. Front.* **2019**, *6*, 1245-1252.

(20) Dutta, B.; Dey, A.; Sinha, C.; Ray, P. P.; Mir, M. H. Photochemical Structural Transformation of a Linear 1D Coordination Polymer Impacts the Electrical Conductivity. *Inorg. Chem.* **2018**, *57*, 8029−8032.

(21) Naskar, K.; Maity, S.; Jana, S.; Dutta, B.; Tanaka, S.; Mallick, D.; Akitsu, T.; Sinha, C. Arylazoimidazole Coordinated and Naphthalene-Dicarboxylato Bridged Polymers of Co(II) and Photochromic Zn(II) Complexes. *Cryst. Growth. Des*. **2018**, *18*, 2986–2997.

(22) Dutta, B.; Jana, R.; Sinha, C.; Ray, P. P.; Mir, M. H. Synthesis of a Cd(II) based 1D coordination polymer by in situ ligand generation and fabrication of a photosensitive electronic device. *Inorg. Chem. Front*. **2018**, *5*, 1998-2005.

(23) Das, S.; Presselt, M. Progress and development in structural and

optoelectronic tunability of supramolecular nonbonded fullerene assemblies. *J. Mater. Chem. C*. **2019**, 10.1039/C9TC00889F.
(24) Lu, K.; Zhao, C.; Luan, L.; Duan, J.; Xie, Y.; Shao, M.; Hu, B. Exploring the role of spin-triplets and trap states in photovoltaic processes of perovskite solar cells. *J. Mater. Chem. C*, **2018**, *6*, 5055–5062.
(25) Dutta, B.; Pratik, S. M.; Jana, S.; Sinha, C.; Datta, A.; Mir, M. H. Novel Br··· π (Chelate) Interaction in a 1D Coordination Polymer Revealing Aromaticity. *ChemistrySelect.* **2018**, *3*, 4289 – 4291.
(26) Li, X.; Cheng, D.; Lin, J.; Li, Z.; Zheng, Y. Di-, Tetra-, and Hexanuclear Hydroxy-Bridged Copper(II) Cluster Compounds: Syntheses, Structures, and Properties. *Cryst. Growth. Des*. **2008**, *8*, 2853-2861.
(27) Wannarit, N.; Siriwong, K.; Chaichit, N.; Youngme, S.; Costa, R.; Moreira, I. P. R.; Illas, F. New Series of Triply Bridged Dinuclear Cu(II) Compounds: Synthesis, Crystal Structure, Magnetic Properties, and Theoretical Study. *Inorg. Chem*. **2011**, *50*, 10648–10659.
(28) Reyes-Ortega, Y.; Alcantara-Flores,J.; Hernandez-Galindo, M.; Ramı´rez-Rosales, D.; Berne`s, S.; Rami´rez-Garcı´a, J.;. Zamorano-Ulloa, R.; Escudero, R. Magnetic Properties and Crystal Structure of a One-Dimensional Phase of Tetrakis (μ2-benzoato O, O ′)-bis (dimethyl sulfoxide) dicopper(II). *J. Am. Chem. Soc*. **2005**, *127*, 16312-16317.
(29) Costa, R.; Lo´pez, C.; Molins, E.; Espinosa, E. Synthesis, Structure, and Properties of a Tetrametallic Ferrocenecarboxylato-Bridged Copper(II) Complex. *Inorg. Chem*. **1998**, *37*, 5686-5689.
(30) Lo´pez, C.; Costa, R.; Illas, F.; Molins, E.; Espinosa, E. Ferromagnetic Copper(II) Complex Containing Ferrocenecarboxylato Bridging Ligands. *Inorg. Chem*. **2000**, *39*, 4560-4565.
(31) Huang, P.-J.; Natori, Y.; Kitagawa, Y.; Sekine, Y.; Kosaka, W.; Miyasaka, H. One-Dimensional Chains of Paddlewheel-Type Dichromium(II,II) Tetraacetate Complexes: Study of Electronic Structure Influenced by σ- and π-Donation of Axial Linkers. *Inorg. Chem*. **2018**, *57*, 5371−5379.
(32) Reger, D. L.; Debreczeni, A.; Smith, M. D. Copper(II) Carboxylate Dimers Prepared from Ligands Designed to Form a Robust π···π Stacking Synthon: Supramolecular Structures and Molecular Properties. *Inorg. Chem*. **2012**, *51*, 1068−1083.
(33) Sil, S.; Datta, J.; Das, M.; Jana, R.; Halder, S.; Biswas, A.; Sanyal ,D.; Ray, P. P. Bias dependent conduction and relaxation mechanism study of Cu_5FeS_4 film and its significance in signal transport network. *J. Mater. Sci*. **2018**, *29*, 5014-5024.
(34) Dökme, İ.; Altındal, Ş.; Gökçen, M. Frequency and gate voltage effects on the dielectric properties of Au/SiO_2/n-Si structures, *Microelectron. Eng*. **2008**, *85*, 1910-1914.
(35) Kamalasanan, M. N.; Kumar, N. D.; Chandra, S. Dielectric and ferroelectric properties of BaTiO3 thin films grown by the sol-gel process. *J. Appl. Phys*. **1993,** *74***,** 5679-5686.
(36) Mukherjee, R.; Dutta, A.; Sinha, T. P. Dielectric Relaxation of Rare Earth Ordered Double Perovskite Oxide Ba_2ErTaO_6. *J. Electron. Mater*. **2016,** *45*, 846-852.
(37) Chanda, S.; Saha, S.; Dutta, A.; Irfan, B.; Chatterjee. R.; Sinha, T. P. Magnetic and dielectric properties of orthoferrites La_{1-x} Pr_xFeO_3 (x = 0, 0.1, 0.2, 0.3, 0.4 and 0.5). *J. Alloys. Compd*. **2015,** *649*, 1260-1266.
(38) Rhoderick, E. H.; Williams, R. H. Metal-Semiconductor Contacts, Clarendon Press, Oxford, 2nd edn, **1988**.
(39) Sze, S. M. Physics of Semiconductor Devices, *Wiley*, New York. **1981**.
(40) Dey, A.; Layek, A.; Roychowdhury, A.; Das, M.; Datta, J.; Middya, S.; Das, D.; Ray, P. P. Investigation of Charge Transport Properties in Less Defective Nanostructured ZnO Based Schottky Diode. *RSC Adv*. **2015,** *5*, 36560-36567.
(41) Das, M.; Datta, J.; Dey, A.; Jana, R., Layek, A.; Middya, S.; Ray, P. P. One step hydrothermal synthesis of a rGO-TiO_2 nanocomposite and its application on a Schottky diode: improvement in device performance and transport properties. *RSC Adv*. **2015,** *5*, 101582-101592.
(42) Jana, R.; Dey, A.; Das, M.; Datta, J.; Das, P.; Ray, P. P. Improving performance of device made up of CuO nanoparticles synthesized by hydrothermal over the reflux method. *Appl. Surf. Sci*. **2018,** *452*, 155-164.
(43) Gupta, R. K.; Yakuphanoglu, F.; Photoconductive Schottky Diode Based on Al/p-Si/SnS_2/Ag for Optical Sensor Applications. *Sol. Energy*. **2012,** *86*, 1539-1545.
(44) Hwang, W.; Kao, K. Electrical transport in solids, Pergamon Press, Oxford/New York, **1981**.
(45) Tasçıoğlu, I.; Aydemir, U.; Altındal, S.; Barrier height fluctuations in InGaN polarization dipole diodes. *J. Appl. Phys*. **2010,** *108*, 064506.
(46) Jain, A.; Kumar, P., S. Jain, C.; Kumar, V.; Kaur, R., Mehra, R. M. Trap Filled Limit Voltage (VTFL) and V^2 Law in Space Charge Limited Currents. *J. Appl. Phys*. **2007,** *102*, 94505-94509.
(47) Soylu, M.; Abay, B. Analysing space charge-limited conduction in Au/n-InP Schottky diodes, Physica E Low Dimens. *Syst. Nanostruct*. **2010,** *43*, 534-538.
(48) Das, M.; Datta, J.; Jana, R.; Sil, S.; Halder,S.; Ray, P. P. Synthesis of rGO-$Zn_{0.8}Cd_{0.2}S$ Via In Situ Reduction of GO For the Realization Of a Schottky Diode With Low Barrier Height and Highly Enhanced Photoresponsivity. *New J. Chem*. **2017,** *41,* 5476-5486.
(49) Middya, S.; Layek, A.; Dey, A.; Datta, J.; Das, M.; Banerjee, C.; Ray,P.P. Role of zinc oxide nanomorphology on Schottky diode properties. *Chem. Phys. Lett*. **2014,** *610*, 39-44.
(50) Sil, S.; Dey, A.; Datta, J.; Das, M.; Jana, R.; Halder, S.; Dhar, J.; Sanyal, D.; Ray, P. P. Analysis of interfaces in Bornite (Cu_5FeS_4) fabricated Schottky diode using impedance spectroscopy method and its photosensitive behaviour. *Mater. Res. Bull*. **2018,** *106*, 337-345.
(51) Datta, J.; Das, M.; Dey, A.; Halder, S.; Sil, S.; Ray, P. P. Network analysis of semiconducting $Zn_{1-x}Cd_xS$ based photosensitive device using impedance spectroscopy and current-voltage measurement. *Appl. Surf. Sci*. **2017,** *420*, 566-578.
(52) Kao, K.C. Dielectric phenomena in solids, Academic press, **2004**.
(53) Nawghare, B. R.; Sakate, S. S.; Lokhande, P. D. A New Method for the Facile Synthesis of Hydroxylated Flavones by Using Allyl Protection. *J. Heterocyclic Chem.* **2014**, *51*, 291-302.
(54) Konda, S. G.; Humne, V. T.; Lokhande, P. D. Rapid and selective deallylation of allyl ethers and esters using iodine in polyethylene glycol-400. *Green Chem.* **2011**, *13*, 2354–2358.

For Table of Contents Use Only

Influence of Axial Linkers on Polymerization in Paddle Wheel Cu(II) Coordination Polymers for the Application of Optoelectronics Devices

Srikanta Jana, Rajkumar Jana, Sayantan Sil, Basudeb Dutta, Hiroki Sato, Partha Pratim Ray,* Ayan Datta,* Takashiro Akitsu, and Chittaranjan Sinha*

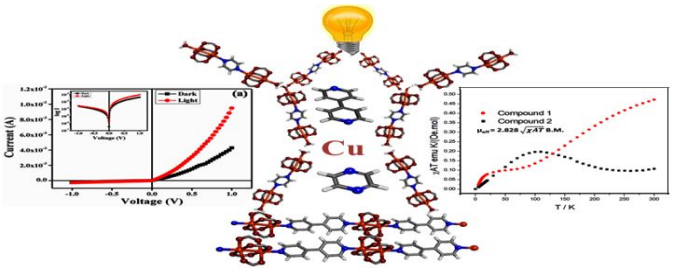

Paddle wheel $[Cu_2(DABA)_4]$ motif is axially ligated with 4,4′-Bipyridine (4,4′-BPY) and Pyrazine (PYZ) to synthesize a 1D and 0D superstructure who exhibit enhancement of electrical conductivity upon light irradiation (Schottky diode device) and the conductivity of **1** is ~150 times higher than **2**. Compound **1** shows higher magnetic moment than the spin only value.